SURFACE CHEMISTRY

Tip-induced flipping of droplets on Janus pillars: From local reconfiguration to global transport

Shile Feng[1,2], Joachim Delannoy[3], Antoine Malod[3], Huanxi Zheng[1], David Quéré[3]*, Zuankai Wang[1]*

Despite their simplicity, water droplets manifest a wide spectrum of forms and dynamics, which can be actuated using special texture at solid surfaces to achieve desired functions. Along this vein, natural or synthetic materials can be rendered water repellent, oleophobic, antifogging, anisotropic, etc.—all properties arising from an original design of the substrate and/or from the use of special materials promoting capillary or elastic forces at the droplet scale. Here, we report an original phenomenon occurring at the tip of asymmetric (half-flat, half-curved) pillars: Droplets reconfigure and get oriented on the curved side of these Janus tips. This local, geometry-driven effect, namely, tip-induced flipping of droplets, is found to be generic and have spectacular global consequences: Vast assemblies of Janus pillars enable a continuous, long-range, and fast self-transport of water harvested from fogs, which makes it possible to collect and concentrate droplets at different scales.

INTRODUCTION

Directional droplet transport is essential in a number of applications, such as microfluidics (*1*–*4*), water harvesting (*5*, *6*), antifogging (*7*, *8*), and thermal or biomedical devices (*9*–*11*). In nature, many living organisms have evolved toward adaptive survival strategies to control droplets. These strategies often rely on the disparity of physical structures and surface energy (*12*–*17*), manifesting in many forms such as wettability gradients (*18*, *19*), anisotropic structures (*20*–*22*), or curvature gradients (*23*, *24*). However, many substrates are hydrophilic, which limits both transport velocity and distance, due to adhesion and friction (*4*, *20*). Conversely, achieving a long-range and fast transport of droplets along nonwetting substrates is challenging. First, nonwetting properties can be destroyed in harsh conditions due to phase change processes (*25*, *26*)—as it happens for instance when microdroplets fill the cavities of a textured surface. Second, nonwetting surfaces have a limited contact with liquids, which minimizes capillary forces. The main driving force for droplets on nonwetting materials arises from coalescence, a way to convert surface energy into kinetic energy, yet in a direction generally normal to the surface—which does not provide motion along the surface (*27*–*29*).

To circumvent these difficulties, we consider a substrate planted with asymmetric pillars that reorient droplets at their tips, a system likely to generate mobility (droplets are mainly facing air) and directionality (owing to the pillar asymmetry). A few natural devices achieve some aspects of this function, and we chose to get inspiration from the botanic world, for which transport of water has to be passive—that is, without the need of external forces. Cases of special interest are cactus spines and pine needles, whose conical shape favors the transport of water along the spines (*30*). Pine needles, specifically, exhibit four kinds of asymmetry, all able to contribute to directional transport of water. As seen in Fig. 1A, needles of *Sabina chinensis* are conical and tilted, with a gradient in height and, last but not least, having a Janus structure opposing flat and curved surfaces. These characteristics are respectively quantified by the cone apex angle ϕ, the tilt angle β, the height gradient α, and the local radius of curvature r of the hemicone found on the side of each needle.

RESULTS

Design principles

Here, we discuss the ability of such texture to transport water harvested from fogs. To that end, we miniaturize the pine needle design and achieve, using three-dimensional (3D) printing with 10-μm resolution, pine needle–inspired asymmetric surfaces (PNAS) with $\phi \approx 10°$, $\beta \approx 70°$, $\alpha \approx 20°$, and $r \approx 100$ μm, as shown in Fig. 1B. Pillars are disposed along a square array with an interpillar distance $s \approx 300$ μm. A sample consists of many parallel stripes, as displayed in the top images in Fig. 1 (B and C). The stripe width $w \approx 1.5$ mm is fixed by the number of pillars of increasing size (Fig. 1, D and E). Water mobility is enhanced by planting on the whole material submicrometric structures of zinc oxide (ZnO) treated with heptadecafluorodecyltripropoxysilane (FAS-17), as shown in the fig. S1. This subtexture on a flat surface provides a typical water contact angle $\theta = 125°$ with a hysteresis of 10° (fig. S2).

As for pine needles, a PNAS surface combines various sources of anisotropy. Figure S3 shows PNAS with height gradients α ranging from 0° to 30°. To decompose their respective effects on water transport, we also build two additional control surfaces using the same techniques of fabrication and coating, where we respectively suppress the gradient in height and the Janus character of the needles. As seen in Fig. 1 (C and D) and fig. S4, Janus needles have all the same height (~400 μm), while tilted cones have no flat side.

First observations

After placing the samples at room temperature (~24°C) in a humid chamber (relative humidity of ~95%), we generate a fog 3 cm above the surface, using an ultrasonic humidifier producing micrometric droplets. The fog first randomly condenses (fig. S5), but Fig. 2 shows that 80 to 90% of the water quickly sit at the texture tops where it continues to grow until it gets ejected when neighboring droplets coalesce. Pillar tips constitute pinning sites for water (*31*, *32*), which explains their tendency to grow there (fig. S6), where they act as obstacles catching the incoming fog. The typical pinning energy of

[1]Department of Mechanical Engineering, City University of Hong Kong, Hong Kong, P. R. China. [2]Key Laboratory for Precision and Non-traditional Machining Technology of Ministry of Education, Dalian University of Technology, Dalian 116024, P. R. China. [3]Physique et Mécanique des Milieux Hétérogènes, UMR 7636 du CNRS, ESPCI, PSL Research University, 75005 Paris, France.
*Corresponding author. Email: david.quere@espci.fr (D.Q.); zuanwang@cityu.edu.hk (Z.W.)

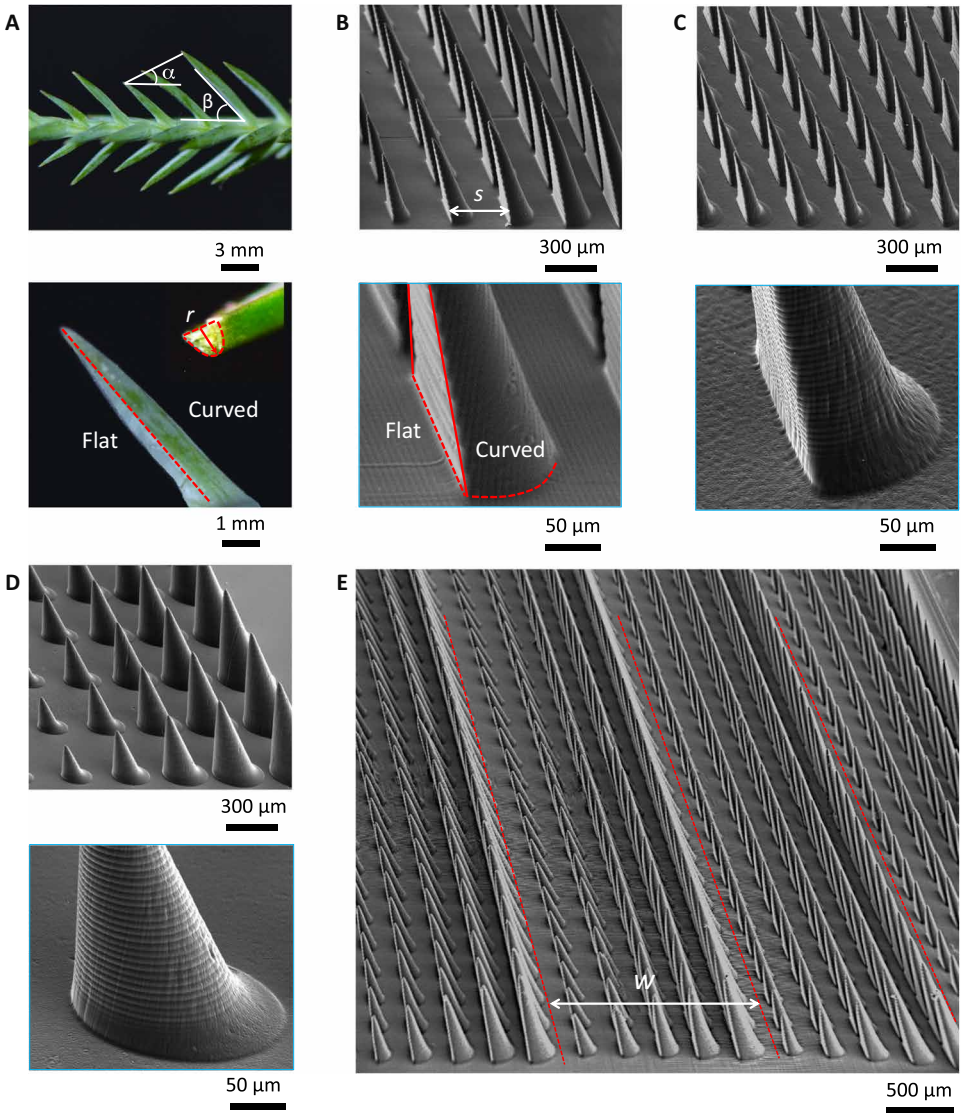

Fig. 1. Geometry of pine needles and of our PNAS arrays. (**A**) Optical images of a pine needle (*S. chinensis*), exhibiting a gradient height $\alpha \approx 30°$ and a tilt angle $\beta \approx 50°$. As shown in the close-up, its two sides are respectively flat and curved, and we denote *r* as the local radius of curvature of the curved side. (**B**) Scanning electron microscopy (SEM) images of our pine needle–inspired asymmetric surface (PNAS), made of tilted ($\beta \approx 70°$) Janus (flat-curved) pillars with a gradient of height $\alpha \approx 20°$ and an interpillar distance $s = 300$ μm. (**C**) SEM images of tilted Janus pillars without gradient of height ($\beta \approx 70°$, $\alpha \approx 0$). (**D**) SEM images of tilted conical pillars with a height gradient ($\beta \approx 70°$, $\alpha \approx 20°$). (**E**) SEM overview of PNAS arrays, showing parallel textured stripes (periodicity $w \approx 1.5$ mm). Other PNAS surfaces are shown in fig. S3, and SEM overviews of Janus and conical surfaces are shown in fig. S4. The total size *L* of each sample is 10 mm. Photo credit: Shile Feng, City University of Hong Kong.

a droplet (with radius *R* and surface tension γ) at the tip scales as $\gamma\phi R^2$. Since the apex angle ϕ of the pillars is much smaller than unity, this quantity is small compared to γR^2, the typical energy of merging: Despite pinning, these summital droplets are mobile enough to be ejected after coalescence.

Droplets are observed in Fig. 2 to self-propel, with marked differences between samples. As seen in the first image in Fig. 2A, water on PNAS mostly sits on the curved side of the pillars (see also fig. S7); in addition, droplets are larger on the right part of the sample, suggesting directional transport toward positive *x*, the direction of increasing pillar height. We can follow the evolution of the pair of droplets highlighted in a dashed circle. After the coalescence of droplets sitting on a same pillar (intrapillar coalescence), the resulting drop jumps to the right and coalesces again, leading to a next jump—a mechanism that takes place until the droplet diameter $2R$ compares to the pillar distance *s* (at $t \approx 9$ ms); afterward, the walk is sustained owing to asymmetric coalescence with droplets on the next needle (interpillar coalescence) (movie S1). The directional motion of water on PNAS takes place at a typical velocity as high as 10 cm/s (fig. S8), owing to low friction associated with a transport occurring either at pillar tips or in air.

The observation of a continuous directional transport arises from the unique design of PNAS. We show in Fig. 2B what happens on Janus structures without gradient in height. As previously, we first observe that droplets at the pillar tips mostly sit on the curved side and get ejected in the $+x$ direction as they coalesce. However, contrasting

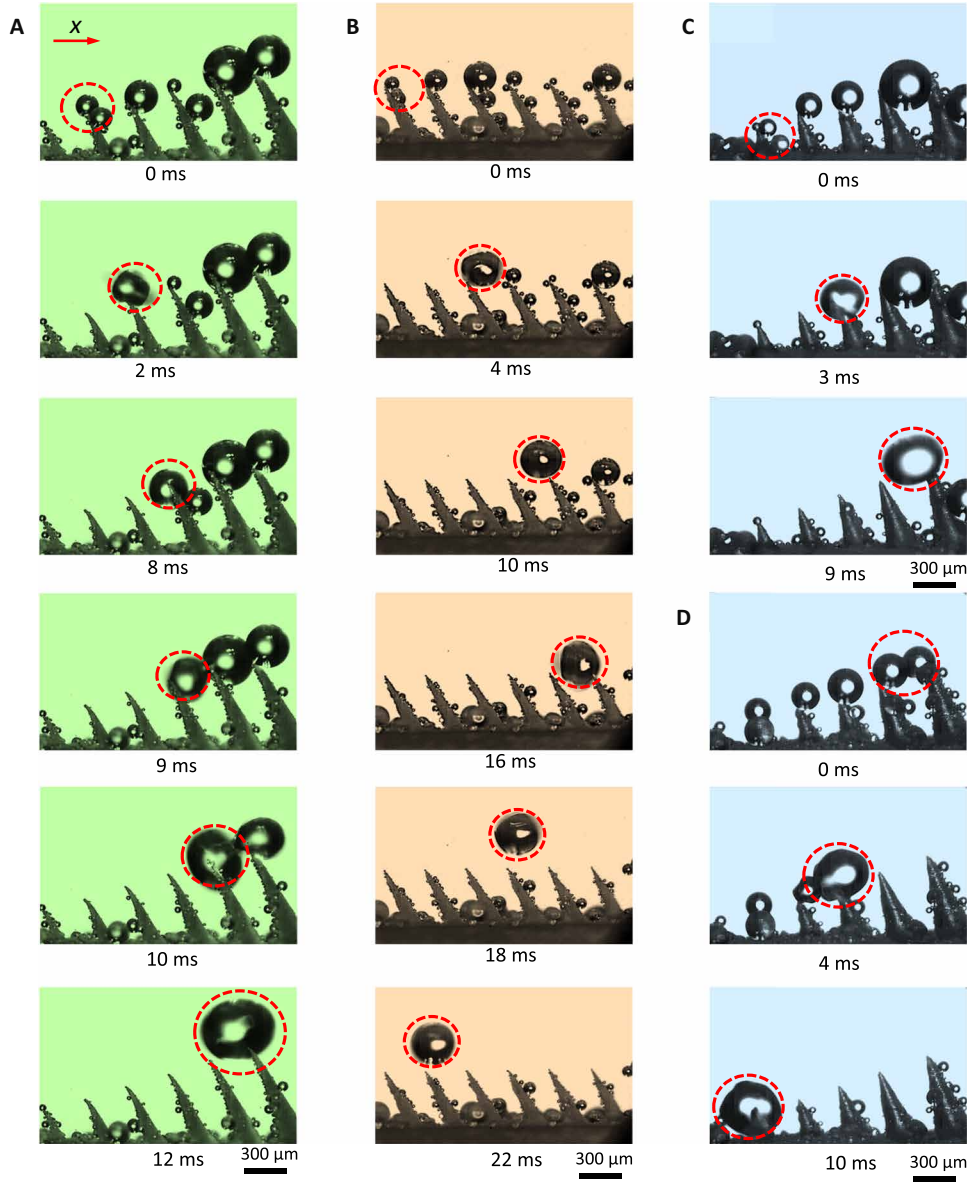

Fig. 2. Droplet transport on the different samples. (**A**) On PNAS, water harvested from a fog self-propels after successive coalescences. Transport takes place along positive *x*, as highlighted by dashes (see also movie S1). (**B**) On equally high Janus pillars, transport starts the same way: Droplets sit on the right side of the Janus pillars and get ejected in the +*x* direction after coalescence. However, interpillar coalescence later launches droplets in the opposite direction (movie S2). (**C** and **D**) On conical needles, coalescence can eject droplets in both +*x* and −*x* directions, due to the absence of orientation of droplets at the needle tips (movies S3 and S4). Photo credit: Shile Feng, City University of Hong Kong.

with PNAS, droplets resulting from an interpillar coalescence can turn back, which emphasizes the role of the height gradient in droplet rectification on PNAS (movie S2). On conical pillars with a gradient of height, droplets sit on any side of the pillars and thus may be launched in both directions, as shown in Fig. 2 (C and D) and movies S3 and S4.

DISCUSSION

The TIF effect

We now compare coalescences at the tips of Janus and conical pillars to illustrate the elementary process that creates the drift of droplets on PNAS, as illustrated in Fig. 3 (A and B). On Janus pillars (Fig. 3A and movies S5 and S6), the resulting drop always flips after coalescence so as to sit on the curved side of the pillar, whatever the ratio between the droplet radii before coalescence. This sharply contrasts with observations on conical pillars (Fig. 3B and movies S7 and S8) where the drop after merging sits on any side, at the location imposed by the Laplace pressure difference between the coalescing droplets, that is, toward the bigger drop. Integrated over all the pillars, this leads to a symmetric distribution of droplets around the cones. Hence, the rectified motion of water in Fig. 3A originates from the Janus nature of the pillars, which serves to overcome the natural tendency of small droplets to empty in large ones and to

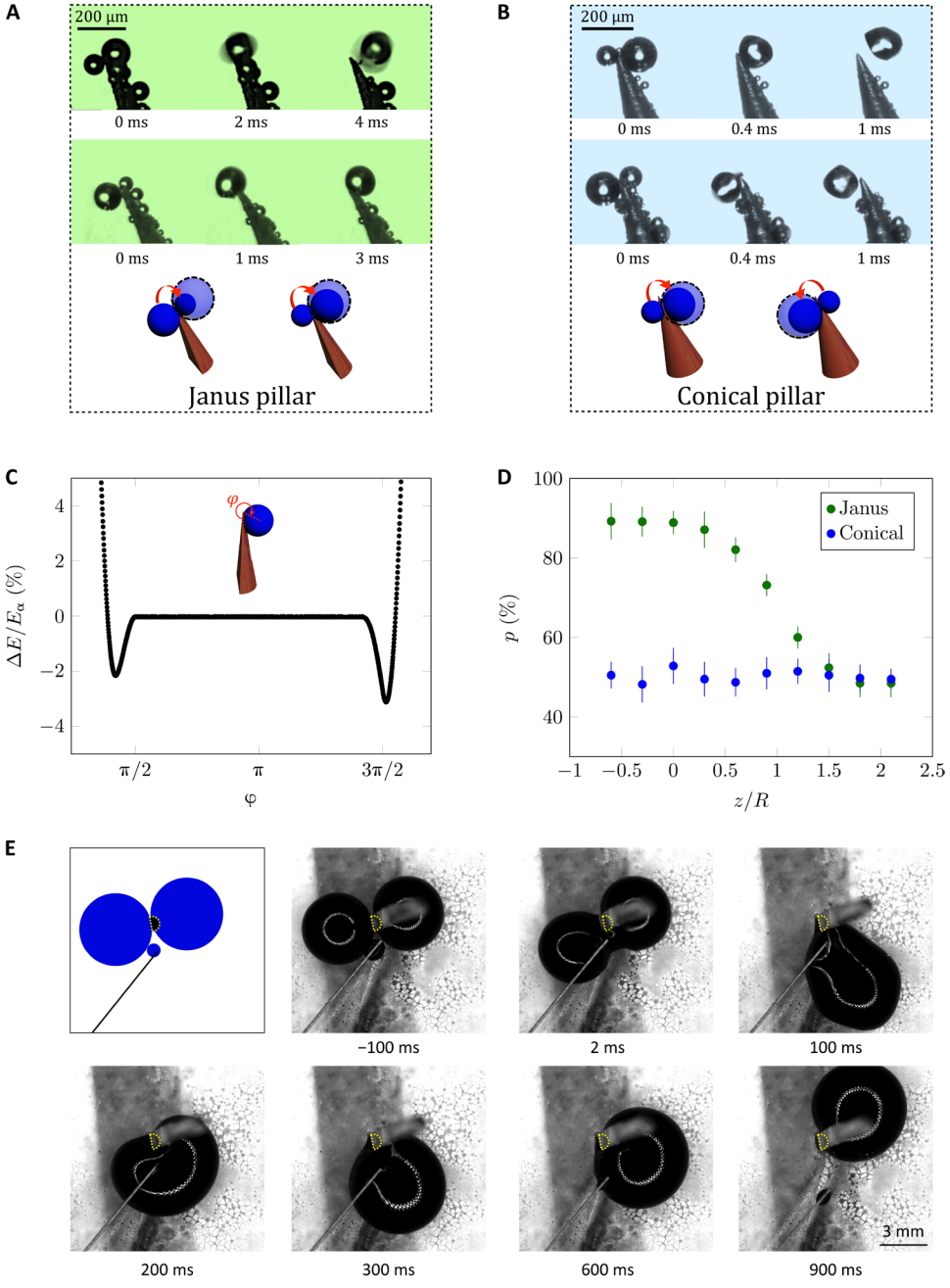

Fig. 3. TIF effect. (**A**) TIF (TIF effect) on Janus pillars: Droplets tend to accumulate at the pillar tip (movie S5), either directly on the curved side of the pillar (first picture) or after flipping from flat to curved (second picture). In the latter case, large droplets can be attracted by small ones, showing that the TIF effect overcomes the difference of Laplace pressure between droplets (movie S6). (**B**) On conical pillars, droplets also gather at the pillar tips, but they sit indifferently on the right or left side of the pillar (movies S7 and S8). Photo credit: Shile Feng, City University of Hong Kong. (**C**) Droplet surface energy (compared to that in air) as a function of φ, the flip angle around the Janus tip. ΔE is normalized by E_a, the adhesion energy of the droplet on a flat solid. (**D**) Probability p to find a droplet on the curved side of a Janus pillar as a function of z/R, the normalized distance to the tip (green data). p is deduced from statistics performed on 200 droplets and compared to the probability of finding droplets on the right side of conical pillars (blue data). (**E**) Sketch and top view of the coalescence of two water drops with $R \approx 2.5$ mm sitting on a superhydrophobic material and placed respectively on the flat and curved sides of a vertical hemicylinder (with $r = 0.5$ mm), whose profile is highlighted with dots. Time starts at the onset of coalescence, after which the merged drop rotates around the solid until it pins on its curved side, confirming the generality of the TIF effect (movie S9). Photo credit: Antoine Malod, ESPCI Paris.

orient the droplets—an original reconfiguration that we call tip-induced flipping (TIF).

Droplet configurations and their corresponding surface energies should be mediated by the morphology of the pillars. We can first compare the surface energy of a small droplet (with size R) sitting either on a flat or a curved surface of larger width ($R < r$). As shown in the Supplementary Materials (fig. S9), we find that the surface energy is always smaller on the flat side, which can be understood as a particular case of the general tendency of drops to move toward the less curved part of a solid (*5*). This classical result sharply contrasts with

Fig. 2 (A and B) and fig. S7 where droplets are systematically observed on the curved side of the pillar, which then imposes the direction of self-propulsion.

This paradox can be understood by considering the spatial confinement induced by the conical character of Janus pillars. A droplet (with size R) at the tip is larger than the pillar width (of order ϕR, with $\phi < 1$). This deeply modifies the energetic landscape around the pillar. Denoting A_{LV} and A_{SL} as the liquid-vapor and liquid-solid surface areas, respectively, we can calculate the surface energy $E = \gamma (A_{LV} - \cos\theta A_{SL})$ of water at a Janus tip (fig. S10). In Fig. 3C, we plot the surface energy $\Delta E = E - 4\pi\gamma R^2$ of a droplet in contact with a pillar compared to that in air, as a function of the flipping angle φ of the liquid around the tip—a rotation that keeps the droplet attached to the tip and thus that is not impeded by pinning. Results are normalized by the adhesion energy E_a of the droplet on a flat, infinite surface (see Supplementary Materials for details). Apart from a flat region where the drop flips above the tip (which provides $\Delta E = 0$), we observe two equilibrium positions respectively on the flat ($\varphi < \pi$) and curved ($\varphi > \pi$) sides. Energy on the curved side is found to be lower than that on the flat side, which successfully explains the tendency of droplets to be asymmetrically disposed on Janus pillars. For a droplet on the flat side, the energy needed to overcome the barrier and to find the absolute minimum is provided by coalescence.

Hence, the TIF effect is a geometric phenomenon sensitive to the droplet size and to the substrate width: If we calculate the surface energy of a droplet as a function of its distance z to the tip, we find that the curved side is favored when z is smaller than a distance of order R (fig. S11). This explains why droplets are mainly found on the curved side of Janus pillars when large enough or close enough to the tip (Fig. 2, A and B). The description is made more quantitative by plotting the probability p to find droplets on a given side of Janus or conical pillars as a function of z (Fig. 3D)—statistics performed in both cases on more than 200 droplets. While p constantly lies around 0.5 for conical pillars (blue data), a strong asymmetry appears on Janus pillars for $z < R$, a situation where the probability for droplets to select the curved side becomes as high as 0.9 (TIF effect). On Janus pillars, p falls to 0.5 for $R < z$, the droplets being then too small to "communicate" across pillars, thereby leading to a random distribution.

We tested the generality of the TIF effect by considering large (millimetric) drops contacting hemicylinders, that is, solids with a flat side and a curved side. As shown in Fig. 3E and movie S9, two water drops ($R \approx 2.5$ mm) sitting on a superhydrophobic surface (to keep them mobile) are placed on the two sides of a vertical hemicylinder (with $r = 0.5$ mm $< R$) and observed from the top. A droplet dispensed by a thin needle is brought in contact with one of the drops (results are independent of which one), so as to induce a bridge between them. After contact, the globule resulting from coalescence is always found to rotate so as to end on the curved side. If we perform the experiment with water drops immersed in a bath of silicone oil with comparable density (to minimize the effects of gravity), we report the same sequence (fig. S12), which emphasizes the generality of the TIF effect on Janus structures (fig. S13 and table S1).

How can we simply understand the TIF effect? As seen in Fig. 3C, calculations indicate that a drop lowers its energy by sitting on the curved side of a Janus pillar rather than on its flat side. We retrieve this effect by considering the elementary situation of a drop (radius R) on a hemicylinder (radius r) (fig. S14). On the flat side, the solid/liquid contact is fixed by the solid width, which yields a surface energy scaling as $\gamma r^2 (1 + \cos\theta)$. In contrast, a droplet on the curved side is constrained by curvature rather than by edges so that longitudinal and transverse contact sizes are $R \sin\theta$ and $[rR (1 + \cos\theta)]^{1/2}$. The corresponding surface energy now scales as $\gamma R^{3/2} r^{1/2} \sin\theta (1 + \cos\theta)^{3/2}$, a quantity smaller than the previous energy for $r < R \sin^{2/3}\theta (1 + \cos\theta)^{1/3}$. Hence, droplets should flip to the curved side of Janus pillars at their tip, where the hemicylinder width is smaller than a distance comparable to the droplet diameter, as reported in Fig. 3D and considered in Fig. 3E.

Long-range rectification

TIF is a geometric, local effect that orients droplets at the pillar tips. It also determines their long-range drift, as evidenced in movies S10 to S12: For intrapillar coalescences, oriented droplets on Janus pillars are ejected obliquely toward positive x, while ejection is random on conical ones. Interpillar contacts also propel water toward $+x$ at the much larger scale of stripes, by taking advantage of the pillar height gradient. In total, most droplets (~85%) on PNAS are driven in the $+x$ direction (fig. S15).

As shown in Fig. 4A, we can also follow the quantity and repartition of water at the global scale of our samples, when exposing the PNAS surface to a fog generated with a constant flux $Q = 15$ µl/s in a circular region of diameter 7.5 mm (dashes in Fig. 4A). The experiment confirms the ability of PNAS to transport directionally a fog at the global centimeter size of the samples, that is, by a distance three

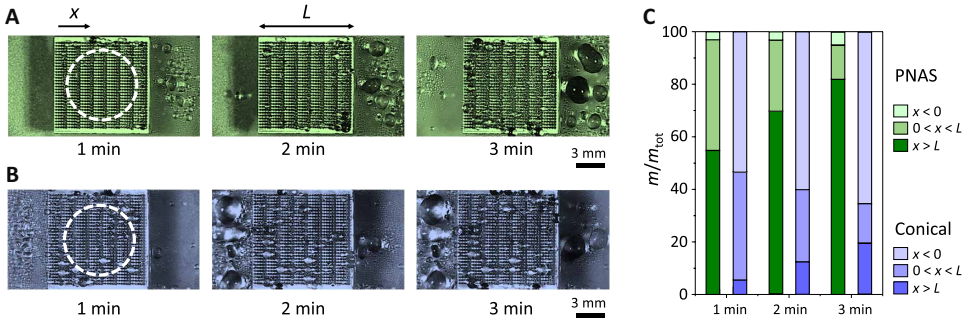

Fig. 4. Large-scale droplet rectification. (**A**) Top view of centimetric samples subject to fog (released 3 cm above the central part, as marked with dashes), as a function of time. PNAS not only rectifies the flux of water droplets but also ejects it out of the rectifying unit. (**B**) Same experiment on inclined conical fibers. Rectification is less efficient and takes place in the opposite direction. Photo credit: Shile Feng, City University of Hong Kong. (**C**) Water repartition $e = m/m_{tot}$ defined as the proportion of the injected water found on the different sections of the sample, that is, $x < 0$, $0 < x < L$, and $x > L$. Repartition is compared on PNAS (green columns) and inclined cones (blue columns) at different times.

orders of magnitude larger than the droplet size. Water is continuously driven in the $+x$ direction, in contrast with Fig. 4B where we follow fog collection on inclined conical fibers. Rectification is then weaker, and it takes place in the $-x$ direction. The repartition of water, defined as the mass m found on the sample normalized by the total mass m_{tot}, can be measured in the regions $x < 0$, $0 < x < L$, and $x > L$, further referred to as regions 1, 2, and 3. We plot in Fig. 4C how the repartition $e = m/m_{tot}$ evolves in space and time on PNAS. Water after 3 min is mostly found in region 3 where we measure $e = 82\%$, to be compared to $e = 5\%$ and $e = 13\%$ in regions 1 and 2. These numbers demonstrate the ability of PNAS to rectify the fog and even to expel it out of the sample—a valuable property to recover water and to avoid the cloaking of the device. In contrast, the ratio e for inclined cones is found to be 20, 15, and 65% in regions 1, 2, and 3, respectively, confirming the existence of an inverted rectification, yet with a smaller efficiency.

The capacity of PNAS to harvest and drive water in a predefined direction arises from the combination of two effects. (i) The TIF effect orients droplets on the curved side of the pillars and thus favors ejection after coalescence in the $+x$ direction, at small droplet scale ($2R < s$). (ii) At a larger scale, the ratchet design of pillars not only favors the displacement to the $+x$ direction but also prevents a backward motion in the $-x$ direction: The highest needles act as an obstacle for droplets brought to the next stripe. As shown in the Supplementary Materials (fig. S16), droplets on tilted Janus pillars with $\alpha = 0$ are rather driven to the $-x$ direction, which is due to the tilt: Droplets at the scale of (or larger than) the pillar spacing are driven after coalescence to the direction of smaller lateral adhesion (*20*, *31*), that is, $-x$.

In summary, we designed a droplet rectifier that achieves continuous directional, long-range, and ultrafast transport of fog droplets by synergistic effects of curvature and height gradients. The main cause of rectification is the TIF effect, a new confinement mechanism that orients droplets at the tips of asymmetric pillars—even in the presence of an adverse Laplace pressure. Our fog rectifier achieves different transport modes, corresponding to different droplet scales, including bottom-to-tip and flat-to-curve transport modes for tiny droplets, jumping-coalescence mode for small droplets, and contact-coalescence mode for large droplets. Despite differences in the transport modes, small and large droplets are found to be entrained in the same direction, which enhances the rectification efficiency of the material. Our work provides new insights ranging from the design philosophy of droplet rectifiers to transport strategies of fogs, which manifests both practical and potential applications in microfluidic devices and water harvesting system.

MATERIALS AND METHODS

Fabrication of pillar arrays with different structure characteristics

We fabricated arrays of tilted pillars having a height gradient and a Janus structure opposing flat and curved surfaces. Samples are built using a projection microstereolithography-based 3D printing technique (BMF Nano Materials Technology Co., Ltd), with 10-μm resolution. In the fabrication process, the model, prebuilt with mapping software, is sliced into a sequence of 2D mask images of predetermined layer thickness followed by an exposure process. We iterate this step for each layer until the entire structure is created. For the as-designed samples, the height gradient is defined by an angle α that can be varied between 0° (no height gradient) and 30°. β, the tilt angle of the pillars defined to the horizontal, can be changed between 60° and 90° (the latter case is that of vertical pillars). The space s between adjacent pillar centers is 300 μm. Pillars are either conical or of a Janus type, with flat and curved sides, and organized in square arrays. We considered three families of sample, with $\alpha = 20°$ and $70° < \beta < 90°$: (i) The sample of interest (so-called PNAS) is inspired by pine needles, and it combines different types of geometrical gradients. In the x direction of the droplet motion, pillar height varies along five successive Janus pillars, and the structure is replicated so that a sample displays parallel stripes with width $w = 5s = 1.5$ mm. (ii) A first control sample (Janus pillars) is equivalent but has no height gradient ($\alpha = 0$): It simply consists of parallel Janus pillars. (iii) A second control sample (conical pillars) is equivalent to the PNAS sample, except that pillars are conical instead of being Janus. All samples are of centimeter size.

Coating the pillars with hydrophobic nanostructures

Samples are planted by ZnO nanostructures using the low-temperature crystal growth method. Crystal seeds are fabricated by mixing $Zn(Ac)_2{\cdot}2H_2O$ (2.2 g) (Shanghai Chemical Reagent Research Institute Co., Ltd.), 20 ml of ethylene glycol monomethyl ether (Shanghai Chemical Reagent Research Institute Co., Ltd.), and monoethanolamine (0.6108 g) (Beijing Chemical Plant, Co., Ltd.), a mixture agitated with a magnetic stirrer for 30 min. For the mother liquor, $Zn(NO_3)_2{\cdot}6H_2O$ (0.74 g) (Shanghai Chemical Reagent Research Institute Co., Ltd.), 1.49 g of $Zn(NO_3)_2{\cdot}6H_2O$ (Shanghai Chemical Reagent Research Institute Co., Ltd.), and hexamethylene tetramine (0.35 g) (Beijing YiLi Fine Chemicals Co. Ltd) are mixed into deionized water (100 ml) and stirred for 30 min. We dip our samples in the crystal seed solution three times and then dry them at room temperature. Subsequently, the sample and mother liquor are placed into agitated reactors, in an oven at 90°C for 10 hours. Last, we treat surfaces with FAS-17 to decrease their surface energy.

Characterizations

The structures of pine needles are observed by digital single lens reflex camera (Nikon, D5200). The micro/nanostructures of micropillar arrays are revealed by scanning electron microscopy (Quanta 450 FEG). A contact angle goniometer (ramé-hart M200 Standard Contact Angle Goniometer) is used to measure the advancing and receding contact angles of water on flat surfaces, which are determined by five individual measurements. The transport dynamics of droplets on samples exposed to fogs is recorded by a high-speed camera (Fastcam SA4, Photron) at the frame rate of 5000 frames per second with a shutter speed of 1/5000 s. Experiments are performed at room temperature with 95% relative humidity. The weight of harvested water is measured with an electronic balance (FA2004N).

SUPPLEMENTARY MATERIALS

Supplementary material for this article is available at http://advances.sciencemag.org/cgi/content/full/6/28/eabb4540/DC1

REFERENCES AND NOTES

1. H. A. Stone, A. D. Stroock, A. Ajdari, Engineering flows in small devices: Microfluidics toward a lab-on-a-chip. *Annu. Rev. Fluid Mech.* **36**, 381–411 (2004).
2. R. Seemann, M. Brinkmann, T. Pfohl, S. Herminghaus, Droplet based microfluidics. *Rep. Prog. Phys.* **75**, 016601 (2012).
3. S.-Y. Teh, R. Lin, L.-H. Hung, A. P. Lee, Droplet microfluidics. *Lab Chip* **8**, 198–220 (2008).
4. Q. Sun, D. Wang, Y. Li, J. Zhang, S. Ye, J. Cui, L. Chen, Z. Wang, H.-J. Butt, D. Vollmer, X. Deng, Surface charge printing for programmed droplet transport. *Nat. Mater.* **18**, 936–941 (2019).

5. Y. Zheng, H. Bai, Z. Huang, X. Tian, F.-Q. Nie, Y. Zhao, J. Zhai, L. Jiang, Directional water collection on wetted spider silk. *Nature* **463**, 640–643 (2010).
6. K.-C. Park, P. Kim, A. Grinthal, N. He, D. Fox, J. C. Weaver, J. Aizenberg, Condensation on slippery asymmetric bumps. *Nature* **531**, 78–82 (2016).
7. Q. Wang, X. Yao, H. Liu, D. Quéré, L. Jiang, Self-removal of condensed water on the legs of water striders. *Proc. Natl. Acad. Sci. U.S.A.* **112**, 9247–9252 (2015).
8. T. Mouterde, G. Lehoucq, S. Xavier, A. Checco, C. T. Black, A. Rahman, T. Midavaine, C. Clanet, D. Quéré, Antifogging abilities of model nanotextures. *Nat. Mater.* **16**, 658–663 (2017).
9. S. Wang, J. S. Lee, M. Wahiduzzaman, J. Park, M. Muschi, C. Martineau-Corcos, A. Tissot, K. H. Cho, J. Marrot, W. Shepard, G. Maurin, J.-S. Chang, C. Serre, A robust large-pore zirconium carboxylate metal–organic framework for energy-efficient water-sorption-driven refrigeration. *Nat. Energy* **3**, 985–993 (2018).
10. S. Amini, S. Kolle, L. Petrone, O. Ahanotu, S. Sunny, C. N. Sutanto, S. Hoon, L. Cohen, J. C. Weaver, J. Aizenberg, N. Vogel, A. Miserez, Preventing mussel adhesion using lubricant-infused materials. *Science* **357**, 668–673 (2017).
11. J.-A. Lv, Y. Liu, J. Wei, E. Chen, L. Qin, Y. Yu, Photocontrol of fluid slugs in liquid crystal polymer microactuators. *Nature* **537**, 179–184 (2016).
12. J. Ju, H. Bai, Y. Zheng, T. Zhao, R. Fang, L. Jiang, A multi-structural and multi-functional integrated fog collection system in cactus. *Nat. Commun.* **3**, 1247 (2012).
13. P. Comanns, G. Buchberger, A. Buchsbaum, R. Baumgartner, A. Kogler, S. Bauer, W. Baumgartner, Directional, passive liquid transport: The Texas horned lizard as a model for a biomimetic 'liquid diode'. *J. R. Soc. Interface* **12**, 20150415 (2015).
14. M. Prakash, D. Quéré, J. W. M. Bush, Surface tension transport of prey by feeding shorebirds: The capillary ratchet. *Science* **320**, 931–934 (2008).
15. H. Chen, T. Ran, Y. Gan, J. Zhou, Y. Zhang, L. Zhang, D. Zhang, L. Jiang, Ultrafast water harvesting and transport in hierarchical microchannels. *Nat. Mater.* **17**, 935–942 (2018).
16. H. Chen, P. Zhang, L. Zhang, H. Liu, Y. Jiang, D. Zhang, Z. Han, L. Jiang, Continuous directional water transport on the peristome surface of *Nepenthes alata*. *Nature* **532**, 85–89 (2016).
17. G.-T. Yun, W.-B. Jung, M. S. Oh, G. M. Jang, J. Baek, N. I. Kim, S. G. Im, H.-T. Jung, Springtail-inspired superomniphobic surface with extreme pressure resistance. *Sci. Adv.* **4**, eaat4978 (2018).
18. M. K. Chaudhury, G. M. Whitesides, How to make water run uphill. *Science* **256**, 1539–1541 (1992).
19. S. Daniel, M. K. Chaudhury, J. C. Chen, Fast drop movements resulting from the phase change on a gradient surface. *Science* **291**, 633–636 (2001).
20. J. Li, X. Zhou, J. Li, L. Che, J. Yao, G. M. Hale, M. K. Chaudhury, Z. Wang, Topological liquid diode. *Sci. Adv.* **3**, eaao3530 (2017).
21. K.-H. Chu, R. Xiao, E. N. Wang, Uni-directional liquid spreading on asymmetric nanostructured surfaces. *Nat. Mater.* **9**, 413–417 (2010).
22. Y. Fang, J. Yong, F. Chen, J. Huo, Q. Yang, J. Zhang, X. Hou, Bioinspired fabrication of bi/tridirectionally anisotropic sliding superhydrophobic PDMS surfaces by femtosecond laser. *Adv. Mater. Interfaces* **5**, 1701245 (2018).
23. J. Ju, K. Xiao, X. Yao, H. Bai, L. Jiang, Bioinspired conical copper wire with gradient wettability for continuous and efficient fog collection. *Adv. Mater.* **25**, 5937–5942 (2013).
24. C. Lv, C. Chen, Y.-C. Chuang, F.-G. Tseng, Y. Yin, F. Grey, Q. Zheng, Substrate curvature gradient drives rapid droplet motion. *Phys. Rev. Lett.* **113**, 026101 (2014).
25. J. Liu, H. Guo, B. Zhang, S. Qiao, M. Shao, X. Zhang, X.-Q. Feng, Q. Li, Y. Song, L. Jiang, J. Wang, Guided self-propelled leaping of droplets on a micro-anisotropic superhydrophobic surface. *Angew. Chem. Int. Edit.* **55**, 4265–4269 (2016).
26. R. D. Narhe, D. A. Beysens, Nucleation and growth on a superhydrophobic grooved surface. *Phys. Rev. Lett.* **93**, 076103 (2004).
27. J. B. Boreyko, C.-H. Chen, Self-propelled dropwise condensate on superhydrophobic surfaces. *Phys. Rev. Lett.* **103**, 184501 (2009).
28. X. Gong, X. Gao, L. Jiang, Recent progress in bionic condensate microdrop self-propelling surfaces. *Adv. Mater.* **29**, 1703002 (2017).
29. H. Li, W. Fang, Y. Li, Q. Yang, M. Li, Q. Li, X. Q. Feng, Y. Song, Spontaneous droplets gyrating via asymmetric self-splitting on heterogeneous surfaces. *Nat. Commun.* **10**, 950 (2019).
30. C. Liu, Y. Xue, Y. Chen, Y. Zheng, Effective directional self-gathering of drops on spine of cactus with splayed capillary arrays. *Sci. Rep.* **5**, 17757 (2015).
31. L. Wang, M. Zhang, C. Gao, Y. Zheng, Coalesced-droplets transport to apexes of magnetic-flexible cone-spine array. *Adv. Mater. Interfaces* **3**, 1600145 (2016).
32. M. Prakash, J. W. M. Bush, Interfacial propulsion by directional adhesion. *Int. J. Non-Linear Mech.* **46**, 607–615 (2011).

Acknowledgments

Funding: We acknowledge the financial support from Research Grants Council of Hong Kong (nos. C1018-17G, 11275216, and 11218417), Shenzhen Science and Technology Innovation Council (no. JCYJ20170413141208098), and Fundamental Research Funds for the Central Universities [DUT19RC(3)055]. **Author contributions:** S.F., Z.W., and D.Q. conceived the research. Z.W. and D.Q. supervised the research. S.F., A.M., and H.Z. carried out the experiment. J.D. and D.Q. built the models. All authors analyzed the data and wrote the paper. **Competing interests:** The authors declare that they have no competing interests. **Data and materials availability:** All data needed to evaluate the conclusions in the paper are present in the paper and/or the Supplementary Materials. Additional data related to this paper may be requested from the authors.

Submitted 25 February 2020
Accepted 22 May 2020
Published 8 July 2020
10.1126/sciadv.abb4540

Citation: S. Feng, J. Delannoy, A. Malod, H. Zheng, D. Quéré, Z. Wang, Tip-induced flipping of droplets on Janus pillars: From local reconfiguration to global transport. *Sci. Adv.* **6**, eabb4540 (2020).